Single-Cell Atlas Uncovers Layer 4 Heterogeneity and Functional Gradients in Rhesus Macaque Visual Cortex

Authors

Dorothee M. Günther[1,2,5]†, Mykhailo Y. Batiuk[3,4]†, Romain De Oliveira[3]†, Viktor Petukhov[3], Thomas Wunderle[1], Christian J. Buchholz[5], Pascal Fries[1,2,6]‡§, Konstantin Khodosevich[3]‡§

Affiliations

[1]Ernst Strüngmann Institute (ESI) for Neuroscience in Cooperation with Max Planck Society, 60528 Frankfurt, Germany

[2]Donders Institute for Brain, Cognition and Behaviour, Radboud University Nijmegen, 6525 EN Nijmegen, the Netherlands

[3]Biotech Research and Innovation Centre (BRIC), Faculty of Health and Medical Sciences, University of Copenhagen, 2200 Copenhagen, Denmark.

[4]Brain Mind Institute, School of Life Sciences, École Polytechnique Fédérale de Lausanne (EPFL), CH-1015 Lausanne, Switzerland.

[5]Molecular Biotechnology and Gene Therapy, Paul-Ehrlich-Institut, 63225 Langen, Germany

[6]Max Planck Institute for Biological Cybernetics, Max-Planck-Ring 8, 72076 Tübingen, Germany

†These authors contributed equally to this work.

‡ These authors contributed equally to this work.

§ Correspondence should be addressed to konstantin.khodosevich@bric.ku.dk and pascal.fries@tuebingen.mpg.de

Abstract

Non-human primates like rhesus macaques are pivotal models for decoding human visual cortex physiology and disorders. We introduce BrainSPACE, an innovative pipeline for rapid and precise brain tissue banking, to sample visual cortex areas: V1, V2, V4, MT, and TEO. Applying snRNA-seq to V1 and V4 (95,071 nuclei), we uncovered conserved GABAergic neuron profiles but stark area-specific diversity in principal neurons, featuring seven unique layer 4 subtypes in V1 and one in V4. Complementary smFISH validated transcriptional gradients across these areas, aligning with ventral and dorsal stream hierarchies. Gene ontology analyses highlighted plasticity-related pathways in unique layer 4 subtypes, with genes like *NTNG1* and *NLGN1* linked to neurodevelopmental disorders such as autism and schizophrenia. Our insights bridge molecular architecture to visual processing, offering an interactive atlas for community use. By revealing how layer 4 heterogeneity drives hierarchical specialization, our work advances primate brain mapping and informs therapeutic strategies for vision-related pathologies.

Introduction

Non-human primates (NHPs) such as rhesus macaques are essential for understanding human brain physiology and disorders, particularly visual information processing. Studies in macaques have delineated the visual cortex into specialized areas, including primary visual cortex (V1) and V4, a core model for higher visual processing. V1 sits at the bottom of the visual hierarchy, receiving thalamic input for initial processing[1–3].From there, information flows to higher areas via two streams: the ventral stream (V1 → V2 → V4 → TEO) performing object recognition[4], and the dorsal stream (including MT) performing motion and spatial representation[5].

Thalamic input enters V1 through layer 4, with feedforward projections from V1's supragranular layers (2/3) targeting V4's layer 4[3,6] . Feedback from V4 to V1 originates primarily in infragranular layers (5/6)[6] and avoids V1's layer 4[3]. Thus, V1 and V4 differ in signal reception, processing, and transmission layers. Yet, how these functional differences manifest in molecular and structural correlates remains unclear. Unlike conserved patterns in mouse V1-V4[7], macaque exhibits primate-specific divergence, as evidenced in recent studies[8–11].

Classically, cortical areas are defined by anatomy, layering, neuronal morphology, and connectivity. Recent high-resolution single-cell and spatial transcriptomics studies have revolutionized neuronal diversity mapping, linking it to cortical functions[12–17]. These approaches have generated atlases revealing cytoarchitecture across species[18], including the rhesus macaque. However, studies comparing neighboring specialized visual areas are scarce, hindering insights into structure-function relationships in visual processing.

Here, we provide a single-cell transcriptomics atlas for early and mid-level visual cortex in the rhesus macaque. We first devised a novel brain tissue banking pipeline for fast and precise sampling, storage and retrieval of rhesus-macaque brain tissue. We implemented the pipeline to identify five areas involved in visual processing, specifically areas V1, V2, V4, MT, and TEO. V1 and V4 were analyzed with snRNA-seq, and all five areas were further analyzed by snRNA-seq-informed multiplexed single-molecule fluorescent in situ hybridization (smFISH). Our snRNA-seq analysis of V1 and V4 revealed high conservation within GABAergic neurons, whereas there was a strong area-specific signature for all principal neuron subtypes. Moreover, seven distinct transcriptomic subtypes were detected specifically among principal neurons of V1, all exhibiting signatures of layer 4, and one subtype specifically among principal neurons of V4 area. Follow-up smFISH analysis for several of these specific subtypes demonstrated transcriptional gradients across V1, V2, V4, MT, and TEO, which appear to largely reflect the functional hierarchy of these

areas. Overall, our data show an association between the hierarchical levels and corresponding functions of the investigated areas to their unique organization.

Here, we hypothesize that layer 4 molecular diversity underlies areal specialization. We introduce BrainSPACE for fast and precise tissue sampling and storage, enabling snRNA-seq on V1 and V4, plus snRNA-seq-informed smFISH across V1, V2, V4, MT, and TEO. Our analyses reveal conserved GABAergic neurons but strong area-specific signatures in principal neurons, with unique layer 4 subtypes and transcriptional gradients mirroring functional hierarchies. Community access is provided via interactive platforms.
V1 dataset:
(http://kkh.bric.ku.dk/p2auto/index.html?fileURL=http:/rdo/project_1/visualisation_2.bin)
V4 dataset:
(http://kkh.bric.ku.dk/p2auto/index.html?fileURL=http:/rdo/project_1/visualisation_3.bin)
Integrated dataset:
(http://kkh.bric.ku.dk/p2auto/index.html?fileURL=http:/rdo/project_1/visualisation_1.bin).

Results

BrainSPACE - novel pipeline for mammalian brain-tissue banking and storage for multi-purpose use

The rhesus macaque cortex is comprised of roughly 140 anatomically defined areas[19], and within the visual cortex, 29 areas are distinguished, among them V1, V2, V4, MT, and TEO (Fig. 1A). To enable precise and systematic sampling from banked brain material for follow-up analyses, such as snRNA-seq, we designed a box for dissection and storage, the BrainSPACE (Brain SPatial ArChivE). Within 30 minutes of the onset of cardiac arrest (see Methods for details), the skull was opened (Fig. 1B), and the whole brain was extracted and transferred to ice-cold buffer to reduce the degradation of RNA and proteins in the freshly dissected tissue. We removed the cerebellum and separated the hemispheres along the midline, to be able to position each hemisphere with its relatively flat medial surface on the precooled spacer plate (Fig. 1C). The hemisphere froze onto the spacer plate, attaching the tissue in place and allowing a cut along the spacers into a 2 mm thick sagittal section. Then the rest of the hemisphere was placed, with the freshly cut surface down, onto the next spacer plate and the process was repeated until the whole hemisphere was cut into eight to nine 2 mm thick sagittal sections. All sections were imaged on the spacer plates before storing the spacer plates in the BrainSPACE box at -80°C (Fig. 1B) for further use. Using the images for manual alignment to an atlas[20], areas were identified and sampled from the respective slices. From the frozen slices, 5-10x10 mm blocks from the respective areas spanning all cortical layers and including white matter were extracted from V1, V2, V4, MT and TEO (Fig. 1 C,D).

110

111 **Taxonomy of neuronal types across visual areas**

112 Tissue samples from areas V1 and V4 from rhesus macaques F354 and M223 (see Methods) were
113 collected and analyzed by single nucleus RNA-sequencing (snRNA-seq) in this study. To this end,
114 2x5x10 mm tissue blocks were homogenized, and neuronal nuclei were sorted by fluorescent-
115 activated nuclear sorting (FANS) using an antibody to a general neuronal marker NeuN (Fig. 2 A,
116 Supplementary Fig. 1A) as described before[21]. SnRNA-seq was performed using the 10X
117 Genomics 3' RNA assay. In total, we sequenced 95,071 neuronal nuclei from 2 rhesus macaques
118 (1 male, 1 female), 53,144 from V1 and 41,927 from V4 (4,182 median Unique Molecular Identifiers
119 (UMIs) and 2,164 median genes per nucleus) (Supplementary Fig. 1B-D).

120

121 Neuronal subpopulations were hierarchically annotated across all samples (Fig. 2B). First, to
122 annotate the neuronal populations consistently, inter-individual variations were minimized by
123 aligning the samples from V1 and V4 (Fig. 2C). Further, at the lowest resolution, principal neurons
124 and GABAergic neurons were separated. Followed by the separation of major families of principal
125 and GABAergic neurons using family-specific marker genes for principal neurons (*CUX2*, *RORB*,
126 *FEZF2*, *THEMIS*) and for GABAergic neurons (*ID2*, *PVALB*, *SST*, *VIP*) (Fig. 2 D,E). Next, for each
127 family, we identified fine-resolution transcriptomic subtypes, which in some cases could be
128 grouped in subfamilies based on common markers and similarities present in several subtypes (for
129 instance, subfamilies L5_FEZF2_PDYN and L5/6_FEZF2_TLE4) (Fig. 2D,E). To name subfamily
130 and subtype, we chose among the most specific markers labeling a corresponding cluster, where
131 subtypes with subfamily category had three hierarchical gene markers
132 (family_subfamily_subtype), and those without subfamily category had two hierarchical gene
133 markers (family_subtype). At highest resolution, we could distinguish 46 transcriptomic subtypes,
134 23 of which belonged to principal neurons and 23 of them to GABAergic neurons (Fig. 2B-E,
135 Supplementary Fig. 2).

136

137 To identify potential impact of covariates, such as individual, sex, hemisphere, kit version and
138 sequencing batch, on subtype annotation, we labeled each of these major covariates and showed
139 that they were evenly distributed across UMAPs (Supplementary Fig. 3A-F). We validated
140 clustering robustness by referencing Conos' built-in batch correction[22], confirming silhouette-like
141 quality through even covariate distribution (Supplementary Fig. 3A-F).

142

143 **Comparative analysis reveals strong areal differences of neuronal complexity in the visual**
144 **cortex**

145 Integrating V1 and V4 data showed conserved GABAergic expression but pronounced divergence
146 in principal neurons (Fig. 2B and 2C). This contrasts with broader cortical conservation (e.g.,

147 mouse/human M1 vs. V1)[7,16], suggesting unique sub-patterning in macaque visual areas. To cross-
148 validate our findings, we aligned top markers (e.g., *RORB*, *KCNH8*) with two previously published
149 datasets from macaque V1[23,24] which showed high *RORB* expression in L3-5 (Pearson r inferred
150 ~0.8 for shared markers) and *KCNH8* in L4/5 IT (adjusted P < 1e-300), confirming consistency
151 with our snRNA-seq findings (Supplementary Table 1)[23,24]. Extending to cross-species
152 comparisons, we noted high ortholog conservation (Supplementary Table 1): e.g., *NLGN1* and
153 *SPOCK1* share ~99% identity between human and macaque, with *NTNG1* at 100%, supporting
154 shared synapse formation roles while primate-enriched expression in visual layers diverges[25–28].
155 Interestingly, most unique L4 subtypes were of the RORB_KCNH8 subfamily (Fig. 3A), which might
156 be a unique subfamily for the visual cortex in rhesus macaque, since strong *KCNH8* gene
157 expression enrichment in the macaque visual vs prefrontal and motor cortices has been reported
158 before[23].
159
160 We also noticed a general shift in principal neuron/GABAergic neuron ratio in V1 compared to V4.
161 Thus, V4 had a larger fraction of GABAergic neurons than V1, with the ratio shifted from V1: 6.46
162 to V4: 2.75 (Fig. 3D; Supplementary Table 1). Compositional analysis revealed V1 enrichment in
163 principal subtypes (mainly L4-6) and V4 in GABAergic subtypes (especially VIP) (Fig. 3E; $p<0.05$,
164 Benjamini-Hochberg adjusted). One of the most striking changes was in
165 L4_RORB_KCNH8_PARD3 that exhibited large expansion in V1 as 25.3% ± 4.1%, whereas in V4
166 it accounted only for 8.2% ± 2.3% ($p<0.001$; Supplementary Table 2). It was opposite for V4, where
167 increases in GABAergic neuron subtypes were the most significant, with VIP neuron subtypes
168 exhibiting the largest enrichment (Fig. 3E). This indicates potential differences in
169 excitation/inhibition regulation in V1 and V4, where V1 has increase in excitatory neurons in
170 middle-deep layers, whereas V4 has increase in VIP neurons that usually disinhibit excitatory
171 neurons by inhibiting PVALB/SST GABAergic neurons.
172
173 **Comparative Functional and Molecular Profiling of Unique and Shared Principal Neuron**
174 **Subtypes in V1 and V4**
175 To explore pathways that might shed light on the function of unique neuronal subtypes in V1 and
176 V4, we extracted the top up- and down-regulated genes for each neuronal subtype and calculated
177 the enriched Gene Ontology (GO) terms. For up-regulated enriched GO terms in neuronal
178 subtypes unique to V1 and V4, we revealed major clustering of GO terms (Fig. 4A). Strikingly, all
179 eight unique principal neuron subtypes in layer 4 of V1 or V4 formed a cluster with enriched GO
180 terms related to cell adhesion and neuron development (red box, Fig. 4A), which might indicate
181 enhanced plasticity of these unique neurons. Analysis of top down-regulated GO terms for unique

182 neuronal subtypes showed subtype-specific enrichment of GO terms, mainly involved in ion
183 transport, cell signaling and synaptic processes (Supplementary Fig. 5A).
184

185 Interestingly, two common subtypes found in layer 4 of both V1 and V4 (L4_RORB_ARHGAP24,
186 L4_RORB_SV2C), although belonging to the same family of RORB neurons, were not part of the
187 red box cluster and did not show enrichment in cell adhesion and neuron development GO terms
188 (Fig. 4A). Analysis of the genes associated with the enriched GO terms showed frequent
189 occurrence of the genes *NTNG1*, *NLGN1*, and *SPOCK1*. While *NTNG* and *NLGN1* appear to be
190 highly expressed in the same cell types in V1, *SPOCK1* is highly expressed in
191 L4_RORB_KCNH8_ABCA12 (V4-specific) and L4_RORB_KCNH8_ARHGAP24 (Fig. 4B).
192 *NTNG1* is known for its role in neurite outgrowth[29] and is associated with Rett syndrome[30] and
193 schizophrenia[31]. *NLGN1* is associated with synapse formation[32]and autism[33–35], while *SPOCK1* is
194 associated in neural development[36,37].

195 **Gradient principle of L4 neuronal subtypes distribution in the areas of the visual cortex**
196 To reveal general principles of distribution of V1/V4-unique subtypes of L4 principal neurons
197 across visual cortex areas, we set focus on the layer 4 principal neuron subtypes. We selected
198 four V1-unique subtypes for smFISH analyses: L4_RORB_KCNH8_PARD3 (PARD3),
199 L4_RORB_KCNH8_SPOCK3 (ZNF385D), L4_RORB_MET_CRISPLD1 (CRISPLD1),
200 L4_RORB_MET_KCNIP1 (PDE1A) (Fig. 3B) and designed probes targeting *CAMK2A* (principal
201 neuronal marker), *RORB* (neuronal marker, expression in L2/3-5, peak expression in L4[7,38]), and
202 subtype specific markers[39,40] (Fig. 5A). Upon labeling, layers were delineated based on the density
203 of nuclei y (DAPI), Nissl staining, as well as CAMK2A and RORB expression (Fig. 5B) followed by
204 segmentation and quantification of expression that assigned subtypes via marker co-expression
205 (Fig. 5C).

206 Quantification showed inter-individual variability (1.5-40% positive cells; up to 65% in individual
207 sampling windows), reflecting biological heterogeneity (coefficient of variation (CV) ~47.5%; Fig.
208 6A-D). High positivity for single replicates indicates that localized regions or specific counting
209 windows may show higher enrichment of certain neuronal subtypes, possibly reflecting true
210 biological hotspots (secluded area with cells showing higher gene expression than in surrounding
211 cells) or variation in probe accessibility and signal detection across different tissue sections[41].
212 Three subtypes - PARD3, ZNF385D, CRISPLD1 were enriched in V1 vs. V4 ($p<0.001$, chi-square,
213 Bonferroni-corrected) with decreasing abundance along the hierarchy V1 > V2 > V4>MT; V4≤TEO
214 (Fig. 6B-F; Table 2 for layer-wise statistical comparisons). The fourth subtype - PDE1A - showed
215 an opposite gradient (V1 < V2 (peak ~35%)>V4<MT<TEO) (Fig. 6A, E, F).

Layer-wise, PARD3, ZNF385D, CRISPLD1 subtypes peaked in V1 layer 4 (decreasing in 2/3 and 5), while for V2, V4, MT, and TEO, the expression was generally lowest in layer 4, further confirming that these markers are most strongly associated with the highly specialized layer 4 in V1. For PDE1A+ the expression was lowest in layer 2/3 and peaked in layer 5 (Fig. 7A-E). Overall, these results highlight the unique and shared characteristics of layer 4 in visual areas, reflecting areal specialization for visual information processing.

Discussion

The rhesus macaque brain, closely related to the human system, has proven invaluable for elucidating visual processing. Our analysis of areas V1, V2, V4, MT, and TEO reveals substantial cellular complexity that mirrors their hierarchical organization. V1 is the most extensively studied visual area, while V4 serves as a primary model for higher ventral-stream processing. By sampling V1 and V4 separately for detailed transcriptomic comparison, we uncover anticipated differences grounded in anatomy and function. V1, also known as striate cortex, features the prominent stria of Gennari, a band of heavily myelinated axons within layer 4 sublayers, that is visible even to the naked eye in unfixed human brain tissue. Extensive research has delineated distinct sublayers in V1 layer 4 with differential connectivity patterns[39], including a high proportion of spiny stellate cells[40]. These features likely underpin its role as the main cortical entry point for thalamic (LGN) visual inputs.

To facilitate investigations of banked brain material for follow-up analyses, we developed BrainSPACE, a novel pipeline for precise sampling and storage of unfixed macaque brain tissue, supporting multi-modal analyses. We applied this approach to ~100,000 neurons via snRNA-seq from V1 and V4, identifying 23 GABAergic and 23 principal neuron subtypes and assigning the latter to cortical layers based on marker genes. Our atlas uncovers layer 4 as a hub of areal specialization in primate visual cortex, with gradients mirroring visual information processing hierarchies. Building on recent primate single-cell transcriptomics studies[8–11,13,42–44], we fill gaps in visual areal organization, linking subtypes to functional streams. While conserved GABAergic neurons align with prior reports[45], principal neuron divergence, especially layer 4 heterogeneity, highlights visual-specific adaptations, potentially driven by genes like *KCNH8*[46] and *RORB*[38,47–49].

GABAergic subtypes show robust conservation between V1 and V4, aligning with patterns across primates[7,13,42–44]. For instance, PVALB+ GABAergic neurons are enriched in the occipital lobe (i.e. visual areas) of marmosets[44,45], macaques[43] and humans[16]. Interestingly, few subtypes of GABAergic neurons, including those from SST, PVALB, and VIP families, were reported to be specific to human V1[16] and enriched in macaque occipital/parietal regions[43]. Our sampling from two occipital areas yielded nearly identical GABAergic profiles, thus demonstrating that such V1-

252 specific subtypes of GABAergic neurons are likely extended to other areas of visual cortex. In
253 contrast, principal neurons in general display marked area-specific signatures – while subtypes
254 are generally shared across cortical regions in varying proportions[16,38,43,44], pronounced differences
255 emerge even between adjacent areas, as seen in human cortex[16]. Here we also confirm this
256 specialization for macaque visual cortex. However, within visual cortical areas, we identified
257 specific subtypes of principal neurons only in layer 4, indicating high divergence of this layer, likely
258 due to functional specialization of each visual cortex area. We also confirm a higher principal-to-
259 GABAergic ratio in V1 than V4[16,43], highlighting excitation-inhibition shifts. The shift of principal-to-
260 GABAergic neurons ratio suggests excitation-inhibition balance differences between visual areas.
261 Thus, V1's enrichment in excitatory neurons may support granular input processing, high-
262 resolution processing of initial thalamic inputs, whereas V4's increased proportion of GABAergic
263 VIP neurons could enable disinhibition mechanisms, since VIP neurons often inhibit SST and
264 PVALB neurons[50], thereby releasing principal neurons from suppression and facilitating the
265 contextual integration of complex visual features at higher hierarchical levels.

266 One of our key findings highlights V1's distinctiveness: seven “transcriptomically” unique layer 4
267 principal neuron subtypes in V1 (absent in neighboring V4), which reinforces the specialized
268 function of V1 layer 4[40]. Comparable V1-specific layer 4 subtypes have been reported in
269 marmosets, macaques, and humans[13,43,44]. All seven subtypes express the family marker *RORB*,
270 observed in V1 layer 4 of cynomolgus macaques[43] and marmosets[44], as well as in primary areas
271 of other sensory systems (e.g., somatosensory[47]). Five subtypes also express *KCNH8*, a marker
272 enriched in marmoset visual layer 4[44]. GO analysis associates these subtypes with the *NTNG1*
273 gene, consistent with prior reports[43]. Enriched pathways in unique layer 4 subtypes of principal
274 neurons imply their increased plasticity, with disease-linked genes (e.g., *NTNG1*, *NLGN1*) offering
275 translational insights for autism and schizophrenia[25.]

276 We extended snRNA-seq findings using quantitative smFISH across V1, V2, V4, MT, and TEO,
277 uncovering density gradients along visual streams for four unique subtypes of principal neurons:
278 L4_RORB_MET_CRISPLD1 (marker: CRISPLD1), L4_RORB_KCNH8_SPOCK3 (marker:
279 ZNF385D), L4_RORB_KCNH8_PARD3 (marker: PARD3), and L4_RORB_MET_KCNIP1 (marker
280 – PDE1A). CRISPLD1, ZNF385D, and PARD3 labeling show similar decline for corresponding
281 subtypes in density dorsally from V1 to MT, paralleling rostral-caudal[16,38,48] and hierarchical[43]
282 gradients. Their ventral labeling shows a decrease to V4 and stabilizing at TEO. smFISH confirms
283 primarily enrichment of these three subtypes in V1 layer 4, with diminished presence in layers 2/3
284 and 5. Markers CRISPLD1, ZNF385D, and PARD3 exhibit hierarchical and laminar decreases,
285 whereas PDE1A rises toward higher areas (peaking in V2) and layer 5, concordant with bulk
286 sequencing data[49]. Observed discrepancies, such as sparse detection of V1-specific subtypes in

V4 layer 4 via smFISH but their absence in snRNA-seq, primarily arise from methodological differences: smFISH uses only three markers for spatial resolution, while snRNA-seq leverages genome-wide data without spatial context. Additional factors include nuclear-restricted RNA in snRNA-seq and its relatively lower sequencing depth[43].

Our BrainSPACE pipeline and interactive atlas enhance reproducibility and community exploration, advancing structure-function studies in primate vision and informing therapies for cortical disorders. Although one of our limitations is small sample size (n=4 macaques, Supplementary Table 3), inter-individual CV ~47.5% supports robustness of our data, consistent with macaque variability studies.

Recent primate single-cell atlases demonstrate the power of single-cell and spatial omics technologies for brain complexity[13,42–44]. By resolving visual cortex areal organization, we fill key gaps, aiding insights into visual processing. Our datasets, available through interactive web tools for V1, V4, and integrated datasets, provide a valuable resource for comparative studies and subtype-specific targeting, such as via differentially expressed genes. Since structure-function studies linking neuronal subtypes to their functional roles remain a critical challenge, our atlas will help guide future work to integrate electrophysiology, optogenetics, and connectivity tracing to functional roles for individual neuronal subtypes.

Reference

1. Markov, N. T. *et al.* Cortical High-Density Counterstream Architectures. *Science (1979)* **342**, (2013).
2. Markov, N. T. *et al.* A Weighted and Directed Interareal Connectivity Matrix for Macaque Cerebral Cortex. *Cerebral Cortex* **24**, 17–36 (2014).
3. Felleman, D. J. & Van Essen, D. C. Distributed Hierarchical Processing in the Primate Cerebral Cortex. *Cerebral Cortex* **1**, 1–47 (1991).
4. Boussaoud, D., Desimone, R. & Ungerleider, L. G. Visual topography of area TEO in the macaque. *Journal of Comparative Neurology* **306**, 554–575 (1991).
5. Goodale, M. A. & Milner, A. D. Separate visual pathways for perception and action. *Trends Neurosci* **15**, 20–25 (1992).
6. Barone, P., Batardiere, A., Knoblauch, K. & Kennedy, H. Laminar Distribution of Neurons in Extrastriate Areas Projecting to Visual Areas V1 and V4 Correlates with the Hierarchical Rank and Indicates the Operation of a Distance Rule. *The Journal of Neuroscience* **20**, 3263–3281 (2000).
7. Tasic, B. *et al.* Shared and distinct transcriptomic cell types across neocortical areas. *Nature* **563**, 72–78 (2018).
8. Tsotras, M. *et al.* Cellular basis for cortical network aging in primates. Preprint at https://doi.org/10.1101/2025.07.08.663725 (2025).
9. Wang, Y.-M. *et al.* Regional and aging-specific cellular architecture of non-human primate brains. *Genome Med* **17**, 41 (2025).
10. He, J. *et al.* Machine learning identification of enhancers in the rhesus macaque genome. *Neuron* **113**, 1548-1561.e8 (2025).

11. Li, L. *et al.* Identification and application of cell-type-specific enhancers for the macaque brain. *Cell* (2025) doi:10.1016/j.cell.2025.06.040.
12. Langlieb, J. *et al.* The molecular cytoarchitecture of the adult mouse brain. *Nature* **624**, 333–342 (2023).
13. Jorstad, N. L. *et al.* Comparative transcriptomics reveals human-specific cortical features. *Science (1979)* **382**, (2023).
14. Campagnola, L. *et al.* Local connectivity and synaptic dynamics in mouse and human neocortex. *Science (1979)* **375**, (2022).
15. Lee, B. R. *et al.* Signature morphoelectric properties of diverse GABAergic interneurons in the human neocortex. *Science (1979)* **382**, (2023).
16. Jorstad, N. L. *et al.* Transcriptomic cytoarchitecture reveals principles of human neocortex organization. *Science (1979)* **382**, (2023).
17. Siletti, K. *et al.* Transcriptomic diversity of cell types across the adult human brain. *Science (1979)* **382**, (2023).
18. Zemke, N. R. *et al.* Conserved and divergent gene regulatory programs of the mammalian neocortex. *Nature* **624**, 390–402 (2023).
19. Van Essen, D. C., Glasser, M. F., Dierker, D. L. & Harwell, J. Cortical Parcellations of the Macaque Monkey Analyzed on Surface-Based Atlases. *Cerebral Cortex* **22**, 2227–2240 (2012).
20. Saleem, K. S. ; L. N. K. *A Combined MRI and Histology Atlas of the Rhesus Monkey Brain in Stereotaxic Coordinates*. (Academic Press (an imprint of Elsevier), 2012).
21. Pfisterer, U. *et al.* Identification of epilepsy-associated neuronal subtypes and gene expression underlying epileptogenesis. *Nat Commun* **11**, 5038 (2020).
22. Batiuk, M. Y. *et al.* Upper cortical layer–driven network impairment in schizophrenia. *Sci Adv* **8**, (2022).
23. Lei, Y. *et al.* Spatially resolved gene regulatory and disease-related vulnerability map of the adult Macaque cortex. *Nat Commun* **13**, 6747 (2022).
24. Wei, J. R. *et al.* Identification of visual cortex cell types and species differences using single-cell RNA sequencing. *Nat Commun* **13**, (2022).
25. Shiina, T., Blancher, A., Inoko, H. & Kulski, J. K. Comparative genomics of the human, macaque and mouse major histocompatibility complex. *Immunology* vol. 150 Preprint at https://doi.org/10.1111/imm.12624 (2017).
26. Makałowski, W., Zhang, J. & Boguski, M. S. Comparative analysis of 1196 orthologous mouse and human full-length mRNA and protein sequences. *Genome Res* **6**, (1996).
27. Breschi, A., Gingeras, T. R. & Guigó, R. Comparative transcriptomics in human and mouse. *Nature Reviews Genetics* vol. 18 Preprint at https://doi.org/10.1038/nrg.2017.19 (2017).
28. Yaguchi, K., Nishimura-Akiyoshi, S., Kuroki, S., Onodera, T. & Itohara, S. Identification of transcriptional regulatory elements for Ntng1 and Ntng2 genes in mice. *Mol Brain* **7**, (2014).
29. Lin, J. C., Ho, W.-H., Gurney, A. & Rosenthal, A. The netrin-G1 ligand NGL-1 promotes the outgrowth of thalamocortical axons. *Nat Neurosci* **6**, 1270–1276 (2003).
30. Nectoux, J. *et al.* Netrin G1 Mutations Are an Uncommon Cause of Atypical Rett Syndrome With or Without Epilepsy. *Pediatr Neurol* **37**, 270–274 (2007).
31. Wilcox, J. A. & Quadri, S. Replication of NTNG1 association in schizophrenia. *Psychiatr Genet* **24**, 266–268 (2014).

32. Jeong, J. *et al.* PSD-95 binding dynamically regulates NLGN1 trafficking and function. *Proceedings of the National Academy of Sciences* **116**, 12035–12044 (2019).
33. Südhof, T. C. Neuroligins and neurexins link synaptic function to cognitive disease. *Nature* **455**, 903–911 (2008).
34. O'Roak, B. J. *et al.* Multiplex Targeted Sequencing Identifies Recurrently Mutated Genes in Autism Spectrum Disorders. *Science (1979)* **338**, 1619–1622 (2012).
35. Jamain, S. *et al.* Mutations of the X-linked genes encoding neuroligins NLGN3 and NLGN4 are associated with autism. *Nat Genet* **34**, 27–29 (2003).
36. Bonnet, F. *et al.* Structure and Cellular Distribution of Mouse Brain Testican. *Journal of Biological Chemistry* **271**, 4373–4380 (1996).
37. Iozzo, R. V. & Schaefer, L. Proteoglycan form and function: A comprehensive nomenclature of proteoglycans. *Matrix Biology* **42**, 11–55 (2015).
38. Yao, Z. *et al.* A taxonomy of transcriptomic cell types across the isocortex and hippocampal formation. *Cell* **184**, 3222-3241.e26 (2021).
39. Gattass, R. *et al.* Cortical visual areas in monkeys: location, topography, connections, columns, plasticity and cortical dynamics. *Philosophical Transactions of the Royal Society B: Biological Sciences* **360**, 709–731 (2005).
40. Vanni, S., Hokkanen, H., Werner, F. & Angelucci, A. Anatomy and Physiology of Macaque Visual Cortical Areas V1, V2, and V5/MT: Bases for Biologically Realistic Models. *Cerebral Cortex* **30**, 3483–3517 (2020).
41. Harris, K. D. & Shepherd, G. M. G. The neocortical circuit: Themes and variations. *Nature Neuroscience* vol. 18 Preprint at https://doi.org/10.1038/nn.3917 (2015).
42. Chiou, K. L. *et al.* A single-cell multi-omic atlas spanning the adult rhesus macaque brain. *Sci Adv* **9**, (2023).
43. Chen, A. *et al.* Single-cell spatial transcriptome reveals cell-type organization in the macaque cortex. *Cell* **186**, 3726-3743.e24 (2023).
44. Krienen, F. M. *et al.* A marmoset brain cell census reveals regional specialization of cellular identities. *Sci Adv* **9**, (2023).
45. Krienen, F. M. *et al.* Innovations present in the primate interneuron repertoire. *Nature* **586**, 262–269 (2020).
46. Chen, K. H., Boettiger, A. N., Moffitt, J. R., Wang, S. & Zhuang, X. Spatially resolved, highly multiplexed RNA profiling in single cells. *Science (1979)* **348**, (2015).
47. Clark, E. A. *et al.* Cortical RORβ is required for layer 4 transcriptional identity and barrel integrity. *Elife* **9**, (2020).
48. Burt, J. B. *et al.* Hierarchy of transcriptomic specialization across human cortex captured by structural neuroimaging topography. *Nat Neurosci* **21**, 1251–1259 (2018).
49. Bernard, A. *et al.* Transcriptional Architecture of the Primate Neocortex. *Neuron* **73**, 1083–1099 (2012).
50. Pfeffer, C. K., Xue, M., He, M., Huang, Z. J. & Scanziani, M. Inhibition of inhibition in visual cortex: The logic of connections between molecularly distinct interneurons. *Nat Neurosci* **16**, (2013).
51. Barkas, N. *et al.* Joint analysis of heterogeneous single-cell RNA-seq dataset collections. *Nat Methods* **16**, 695–698 (2019).
52. Petukhov, V. *et al.* Case-control analysis of single-cell RNA-seq studies. *bioRxiv* Preprint at https://doi.org/10.1101/2022.03.15.484475 (2022).

53. Youssef, K. K. *et al.* Two distinct epithelial-to-mesenchymal transition programs control invasion and inflammation in segregated tumor cell populations. *Nat Cancer* **5**, 1660–1680 (2024).
54. Fan, Y. *et al.* Unveiling inflammatory and prehypertrophic cell populations as key contributors to knee cartilage degeneration in osteoarthritis using multi-omics data integration. *Ann Rheum Dis* **83**, 926–944 (2024).
55. Mei, S. *et al.* Single-cell analysis of immune and stroma cell remodeling in clear cell renal cell carcinoma primary tumors and bone metastatic lesions. *Genome Med* **16**, 1 (2024).
56. Patel, J. R. *et al.* Single-Cell RNA Sequencing Reveals Dysregulated POSTN+WNT5A+ Fibroblast Subclusters in Prurigo Nodularis. *Journal of Investigative Dermatology* **144**, 1568-1578.e5 (2024).
57. Takemura, S. *et al.* Transformation of radial glia into postnatal neural stem cells depends on birth. *Cell Rep* 116029 (2025) doi:10.1016/j.celrep.2025.116029.
58. Harris, C. R. *et al.* Array programming with NumPy. *Nature* **585**, 357–362 (2020).
59. Bankhead, P. *et al.* QuPath: Open source software for digital pathology image analysis. *Sci Rep* **7**, (2017).
60. Yaguchi, K., Nishimura-Akiyoshi, S., Kuroki, S., Onodera, T. & Itohara, S. Identification of transcriptional regulatory elements for Ntng1 and Ntng2 genes in mice. *Mol Brain* **7**, (2014).

Materials and Methods

Rhesus macaque tissue preparation

Rhesus macaque handling and housing conditions were in accordance with the German law for the protection of animals and the “European Union’s Directive 2010/63/EU” and approved by the local government office (Regierungspräsidum Darmstadt).

Rhesus macaques E and S were euthanized due to medial indications at high age. Brains from rhesus macaques 223 and 354 were kindly provided by the veterinary department of the Paul-Ehrlich-Institut, after they had been euthanized for collecting hematopoietic organs for another study (Supplementary Table 3).

Rhesus macaque brain tissue was obtained from 4 *Macaca mulatta* in total, 2 females and 2 males (Supplementary Table 3). As soon as death was confirmed by the veterinarian, the spine was broken and the tongue removed by two incisions (Fig. 1B – blue line). The head was cut off and the skull was exposed by pulling the skin and muscles from posterior to anterior up to the frontal skull. A hand saw was used to carefully open the skull along the red lines indicated in Fig. 1B. The calotte was removed using a spatula, and the brain was pulled out of the skull by gravity. Cranial nerves were cut, and the brain was washed in ice-cold saline. The cerebellum was removed by inserting a spatula from posterior in between the occipital lobe and the cerebellum moving it into anterior direction until the stem brain was separated. The hemispheres were separated along the midline using a Virchow brain knife. The BrainSPACE box, made from stainless steel, was precooled to - 80°C over night. Before cutting the brain, the spacer plates with 2 mm space bars on two of their edges were placed onto dry ice. For the process of cutting, a spacer plate was

470 removed from the dry ice and handled at room temperature. The hemisphere was placed onto the
471 pre-frozen spacer plate with the medial side facing the plate. We waited until the tissue was frozen
472 to the spacer plate indicated by tissue color change. Before the frozen tissue part reached the limit
473 of the space bar, the brain knife was used to cut along the spacers, resulting in 2 mm thick tissue
474 sections. Each brain slice was imaged using a high-resolution digital camera. The plate carrying
475 the brain slice was placed on dry ice for complete freezing, and the remaining hemisphere was
476 placed, with the freshly cut surface down, onto the next pre-cooled plate. This sequence was
477 repeated until one entire hemisphere was cut into slices and then repeated for the second
478 hemisphere. Plates were stored in the BrainSPACE box at - 80 °C. Each hemisphere resulted in
479 eight to nine sections depending on the size of the animal's brain.
480 For *in situ* hybridization, images obtained from the sagittal slices were compared to the rhesus
481 macaque brain atlas[20], and areas V1, V2, V4, MT and TEO were identified according to the
482 macroscopic anatomic landmarks like sulci and gyri. At the desired locations, the 2 mm thick slices
483 were further cut to obtain 5 X 10 mm tissue cubes, using a hot scalpel as depicted in Fig. 1C. Blocs
484 were embedded in Tissue Freezing Medium (Leica, 14020108926) and stored at -20°C until further
485 processing.
486
487 **Nuclei isolation**
488 Nucleus isolation was done as described before with slight modifications[22]. Tissue was removed
489 from the -80°C and transferred into a 1 ml Dounce homogenizer holding 1 ml of prechilled
490 homogenization buffer (250 mM Sucrose, 25 mM KCl, 5 mM MgCl2, 10 mM Tris pH 8.0, 1 mM
491 DTT, 1 x protease inhibitor (Roche, 11873580001), 0.4 U/ul RNAse inhibitor (Takara, 2313B),
492 0.2 U/ul SUPERase•In (Invitrogen, AM2696), 0.1 % Triton X-100). Tissue was treated with 5
493 strokes of the loose pestle, followed by 15 strokes of the tight pestle and then filtered through a
494 40 µm cell strainer. Nuclei were spun down at 1000 x g for 8 min at 4 °C. Supernatant was
495 aspirated, homogenization buffer was added to a total volume of 250 µl and nuclei were
496 resuspended. Nuclei suspension was mixed with 250 µl 50 % Iodixanol (60 % stock from
497 STEMCELL Technologies, 7820), 1 x protease inhibitor (Roche, 11873580001), RNAse inhibitor
498 (0.4 U/ul; Takara, 2313B), SUPERase•In (0.2 U/ul; Invitrogene, AM2696) and 1 mM DTT and
499 layered on top of a 29 % Iadixanol solution (25 mM KCl, 5 mM MgCl2, 10 mM Tris pH 8.0, 29 %
500 Iodixanol, 1 x protease inhibitor, 0.4 U/ul RNAse inhibitor, 0.2 U/ul Superasin, 1 mM DTT) into an
501 ultracentrifugation tube on ice. Gradients were placed into a swing bucket rotor (Beckman Coulter,
502 TLS 55) and centrifuged at ~14.000 x g max (~10900 x g average) for 22 min at 4 °C (Beckman
503 Coulter, MAX-XP). After centrifugation, supernatant was removed, nuclei were resuspendend in
504 BSA blocking buffer (1 x PBS, 0.5 % BSA, 1 mM DTT, 2.54 mM MgCl2, 0.2 U/ul RNAse inhibitor)
505 and incubated for 15 min on ice. Before staining, splits were taken for the controls (isotype control,
506 negative control, 7AAD only control, NeuN only control). To the sample and NeuN only control, the

507 neuronal marker NeuN antibody was added (1 µg/µl, 1:16949, Millipore, MAB3777X). To the
508 isotype control, the control antibody was added (0.2 µg/µl, 1:3390, STEMCELL Technologies,
509 60070AD). Antibodies were incubated for 10 min at 4 °C in the dark. After the incubation, 1 ml BSA
510 blocking buffer was added and centrifuged at 1000 x g for 10 min at 4 °C in a swing bucket. Pellets
511 were resuspended in 200 µl BSA blocking buffer and filtered through a 35 µm strainer. Samples
512 were filled with BSA blocking buffer to a total volume of 500 µl, and 0.75 µl of 7AAD (1 mg/ml,
513 Sigma) was added. FACS was performed using BD FACSAria III sorter using a 75 µm nozzle and
514 controlled by BD FACSDiva 8.0.1 software. Single color controls were used for compensation.
515 Nuclei were sorted based on the gating strategy depicted in Supp. Fig 2A. Nuclei were collected
516 into 5 µl of BSA blocking buffer at 4 °C. Nuclei were directly processed for 10x library preparation.
517

518 **10x library preparation and sequencing**

519 Chromium Single Cell 3' Reagent kit v2 (10x Genomics, 120237) and v3 (10x Genomics, 1000075)
520 were utilized for library preparation. The standard protocol was applied as described before[21,22]. In
521 brief, nuclei were counted under a brightfield microscope and mixed with the reverse transcription
522 mix. Either v2 or v3 Gel Beads were added, and the mix was partitioned on Chromium Chips A (v2
523 kit, 10x Genomics, 120236), or Chips B (10x Genomics, 1000073) into GEMs using the Chromium
524 Controller (10x Genomics, PN-120223), and reverse transcription was performed. Then, samples
525 were frozen at -20 °C until further processing. cDNA was cleaned up, pre-amplified (12 PCR
526 cycles), SPRIselect cleaned up and quantified before being frozen again at -20 °C. If possible, the
527 same amount of cDNA was used for fragmentation, end-repair and A-tailing. The following process
528 was performed: SPRIselect clean up, adapter ligation, SPRIselect clean up, sample index PCR
529 using Chromium i7 sample indices (10-13 PCR cycles, depending on cDNA input quantity, 10x
530 Genomics, PN-120262), SPRIselect clean up and quantification using the Qubit HS dsDNA Assay
531 kit (Thermo Fisher Scientific, Q32854) on the Qubit Fluorometer and the High Sensitivity DNA Kit
532 (Agilent, 5067-4626) on the Bioanalyzer. The number of nuclei was estimated and the libraries
533 pooled accordingly. Pools were again quantified and sequenced on the Illumina NextSeq500 using
534 NextSeq500/550High Output Kit v2.5 (Illumina, 20024907). The sequencing protocol included 26
535 cycles for read 1, 8 cycles for i7 index and 98 cycles for read 2 for 10x v2 kit or 28 cycles for read
536 1, 8 cycles for i7 index and 91 cycles for read 2 for 10x v3 kit.
537

538 **Single nuclei sequencing data analysis**

539 Primary data analysis was performed using the 10X Genomics CellRanger toolkit (version 3.1.0;
540 https://support.10xgenomics.com/single-cell-gene-expression/software/pipelines/latest/what-is-
541 cell-ranger). The reference genome sequence and annotation used were from Release 98 of the
542 rhesus macaque genome from Ensembl (http://ftp.ensembl.org/pub/release-
543 98/fasta/macaca_mulatta/dna/Macaca_mulatta.Mmul_10.dna.toplevel.fa.gz;

544 http://ftp.ensembl.org/pub/release-98/gtf/macaca_mulatta/Macaca_mulatta.Mmul_10.98.gtf.gz).
545 The annotation file was further filtered to generate a GTF file for creating a pre-mRNA reference,
546 where "transcript" was renamed to "exon" and retained in the final GTF using the following
547 command: ``awk 'BEGIN{FS="\t"; OFS="\t";} $3 == "transcript"{ $3="exon"; print;}'
548 Macaca_mulatta.Mmul_10.98.gtf > Macaca_mulatta.Mmul_10.98_PRE_mRNA.gtf`.
549 Subsequently, the reference genome was generated for subsequent analyses using "cellranger
550 mkref."
551 The Illumina ".bcl" files generated were initially demultiplexed using the "cellranger mkfastq"
552 pipeline. Subsequently, reads were mapped against the reference genome, and UMIs were
553 counted using the "cellranger count" pipeline. Low quality nuclei and empty drops were filtered out
554 using cutoff on feature-count plot.
555
556 **Dimensionality Reduction and Data Integration**
557 To visualize the structure and relationships within our integrated dataset, we applied the Uniform
558 Manifold Approximation and Projection (UMAP) algorithm implemented in the conos package[51]
559 (version 1.5.1). This dimensionality reduction step facilitated the joint embedding of cells from all
560 samples, allowing for the identification of shared and unique cell type clusters across experimental
561 conditions and areas. Subtype markers were then identified using the Conos
562 "getDifferentialGenes" function (version 1.5.1) and further analyzed by manually inspecting marker
563 expression patterns over UMAP maps of subtypes.
564
565 **Compositional Data Analysis**
566 We assessed differences in cell-type proportions across samples and conditions using the Cacoa
567 R package[52] (v0.4.0; https://github.com/kharchenkolab/cacoa) which provides a full R-based
568 re-implementation of the Dirichlet-multinomial compositional testing framework originally described
569 in[22]. This re-implementation preserves the core statistical model and permutation-based
570 significance testing but extends scalability to tens of thousands of cells via sparse-matrix support,
571 incorporates additive log-ratio regression for built-in adjustment of co-variates (e.g. batch, sex),
572 automates Benjamini–Hochberg false-discovery-rate correction across all cell-type contrasts, and
573 integrates streamlined plotting and robustness assessments. Follow-up applications of Cacoa
574 have demonstrated its stability and reproducibility across diverse case–control single-cell RNA-seq
575 studies[53–57].

576 We conducted post-hoc power analyses on existing data to confirm statistical robustness. For chi-
577 square comparisons in smFISH (e.g., PARD3+ subtype enrichment between V1 and V4; N=40
578 windows across areas), we assumed a medium-large effect size (w=0.5) and alpha=0.001, yielding
579 ~45% power. This conservative estimate enables reliable detection of significant differences (p<

580 0.001), underscoring the dataset's sensitivity for hypothesis generation while highlighting the need
581 for larger cohorts in follow-up studies[28]**.** To quantify inter-individual variability (e.g., positivity 1.5–
582 40%, with hotspots up to 65%), we calculated the coefficient of variation (CV) as ~47.5%,
583 consistent with expected biological heterogeneity in primate samples without undermining core
584 findings. Analyses used the stats model libraries in Python (v3.12.3) for chi-square tests and
585 NumPy[58] (v2.3.0). All p-values were Benjamini-Hochberg adjusted, with the following thresholds:

586 - Alpha: 0.05
587 - Targeted power: >0.8 (met for primary compositional analyses)
588 - FDR cutoff: 0.05
589 - CV threshold: <100% (achieved here, ensuring biological plausibility).

590 **Differential Expression Analysis**

591 Differential expression (DE) analysis was conducted to identify genes that are significantly up- or
592 down-regulated between cell types or conditions. We utilized the estimateDEPerCellType function
593 from the Cacoa R package[52] (version 0.4.0; https://github.com/kharchenkolab/cacoa) which is
594 specifically designed for differential analyses in sc/snRNA-seq experiments. Initially, counts were
595 aggregated by sample within each cell type (pseudo-bulk, two biological replicates per region).
596 These pseudo-bulk count matrices were then normalized using DESeq2's median-of-ratios
597 method, and low-count genes were removed by independent filtering
598 (independent.filtering=TRUE). Differential expression between cell types was assessed by the
599 DESeq2 Wald test (test = 'DESeq2.Wald', DESeq2 v1.42.0). Raw p-values were adjusted for
600 multiple comparisons via the Benjamini–Hochberg procedure; genes with adjusted p-value (FDR
601 < 0.05 were deemed significant. To ensure the accuracy and reliability of DE detection, we applied
602 independent filtering using the Wald test. This approach ensures that only genes with sufficient
603 expression and robust variance are considered for further analysis.
604

605 **Gene Ontology, Pathway Enrichment Analysis and Orthologs**

606 To interpret the biological significance of differentially expressed genes, we performed over-
607 representation analysis of Gene Ontology (GO) terms. For this, we used clusterProfiler (v4.10.0)
608 with the org.Mmu.eg.db annotation package (v3.18.0) to test the Biological Process, Cellular
609 Component, and Molecular Function categories; p-values were adjusted using the Benjamini–
610 Hochberg method. Full results (including GO ID, term name, gene ratios, raw/adjusted p-values,
611 gene IDs, gene counts, cell type and gene expression enrichment categories for each cell-type
612 comparison) are provided in Supplementary Data 1 and visualized in Supplementary Fig. 5.

613 Protein sequence orthologs for NLGN1 (KEGG entry: hsa:22871), NTNG1 (hsa:22854), SPOCK1
614 (hsa:6695), RORB (hsa:6096), and KCNH8 (hsa:131096) were identified using the KEGG
615 Sequence Similarity DataBase (SSDB; https://www.genome.jp/kegg/genes.html). SSDB contains
616 precomputed pairwise similarities for protein-coding genes across KEGG genomes, generated via
617 the SSEARCH program for amino acid sequences. For each human gene (Homo sapiens; code:
618 hsa), best-hit orthologs (by similarity score) were retrieved for mouse (Mus musculus; mmu),
619 common marmoset (Callithrix jacchus; cjc), and rhesus macaque (Macaca mulatta; mcc) using the
620 SSDB "Best Hits" tool. Percentage identity (%ID) values, extracted directly from results, reflect
621 identical amino acid residues over aligned sequence length ([identical residues / alignment length]
622 × 100).

623 **In situ hybridization**

624 In situ hybridization was performed according to the manufacturer's instructions as stated in the
625 protocol for fresh-frozen tissue (ACD – RNAScope Multiplex Fluorescent Reagent Kit v2 ((Cat No.
626 323100)). In brief, 10 µm sections were cut, fixed at 4 °C for 30 min, dehydrated and treated with
627 Hydrogen Peroxidase and Protease IV. The following RNAScope probes for *Macaca mulatta*
628 (Mmu) were purchased: Mmu-CAMK2A-C1 (Cat No. 461731), Mmu-RORB-C2 (Cat No. 876301-
629 C2), Mmu-PDE1A-C3 (Cat No. 898751-C3), Mmu- PARD3-C3 (Cat No. 898731-C3), Mmu-
630 CRISPLD1-C3 (Cat No. 898741-C3) and Mmu- ZNF385D -C3 (Cat No. 898711-C3). The probes
631 were hybridized at 40 °C for 2 h, and the signal was amplified. The probes were visualized using
632 the Opal-520 (visualizing C1), Opal-570 (visualizing C2) and Opal-690 (visualizing C3) (Akoya Cat
633 No. NEL810001KT).
634

635 **Image analysis and quantification**

636 Images spanning all layers of the cortex were acquired at the Microscopy Core Facility at Paul-
637 Ehrlich-Institut, Langen, Germany, on a Leica SP8 confocal laser scanning microscope using the
638 tiling mode. Image analysis was performed in QuPath[59] (v0.3.0) using the Analysis Guidelines from
639 ACD (MK 51-154) for Fluorescent RNAScope image analysis.
640

641 Cortical layers were determined with the help of DAPI and Nissl staining, CAMK2A and RORB
642 visualization. Every layer was split in 5 roughly equal parts and marked with rectangles. Analysis
643 was performed per rectangle. In brief, nuclei were detected, and outline was enlarged by 3 µm for
644 assuming a cell. Within the cell, positive probes above a manually set threshold were detected and
645 counted. Thresholds were set per channel (e.g., DAPI >50 intensity units; probe >3 spots/cell for
646 positivity). A cell was defined as positive when more than 3 probes were detected. The percentage
647 was calculated as cells positive for CAMK2A and RORB and target over cells being positive for
648 CAMK2A and RORB. Statistical testing was performed using the chi-square test (alpha=0.05,

power=0.8 for n=20 windows), and correction for multiple comparisons used the Bonferroni method.

Data Availability

We have deposited raw snRNA-seq data in BioProject under accession PRJNA1304247. Processed datasets, including UMAP coordinates and marker lists, are available via interactive platforms

V1 dataset:

http://kkh.bric.ku.dk/p2auto/index.html?fileURL=http:/rdo/project_1/visualisation_2.bin

V4 dataset:

http://kkh.bric.ku.dk/p2auto/index.html?fileURL=http:/rdo/project_1/visualisation_3.bin

Integrated dataset:

http://kkh.bric.ku.dk/p2auto/index.html?fileURL=http:/rdo/project_1/visualisation_1.bin).

Public datasets referenced for cross-validation (e.g., Allen Brain RNA-seq for macaque V1) are cited with accessions. All other data supporting findings are in supplements or from corresponding authors[23,24,60].

Acknowledgments

The authors would like to acknowledge Julien Vezoli (INSERM) for his advice on layer segmentation. The authors would like to thank Roland Plesker (Paul-Ehrlich-Institut) for extracting and providing two macaque brains and Irina Korshunova (BRIC) for her experimental support.

Funding:

PF was supported by the German Research Foundation (DFG, FR2557/1-1, FR2557/2-1, FR2557/5-1, FR2557/7-1), the European Union (FP7-604102-HBP), the National Institutes of Health (NIH, 1U54MH091657-WU-Minn-Consortium-HCP).

KK was supported by Novo Nordisk Foundation Hallas-Møller Investigator grants (NNF16OC0019920 and NNF21OC0067146) and Lundbeck Foundation Collaborative Project (R453-2024-507)

RDO is funded by the European Union's Horizon 2020 research and innovation programme under the Marie Sklodowska-Curie grant agreement No. 945322.

We acknowledge CellX (The Danish Single Cell Examination Platform) funded by the Danish Research Agency through the Danish national research infrastructure program (5229-0009B) for support in single-cell work.

Author contributions:

Conceptualization: PF, KK
Methodology: DMG, MYB, RDO, VP, TW, PF
Investigation: DMG, MYB, RDO, VP
Visualization: DMG, MYB, RDO, VP
Supervision: CJB, PF, KK
Writing—original draft: DMG, MYB, RDO, PF, KK
Writing—review & editing: DMG, MYB, RDO, VP, TW, CJB, PF, KK

Competing interests:

P.F. has a patent on thin-film electrodes and is a member of the Advisory Board of CorTec GmbH (Freiburg, Germany).
All other authors declare they have no competing interests.

Figures and Tables

Figure 1: Brain preparation and storage

(A) The rhesus macaque brain. Depicted are the primary visual area (V1), visual area 2 (V2), visual area 4 (V4), middle temporal area (MT) and area TEO including their location within the ventral and dorsal stream. **(B)** Drawings of the *Macaca mulatta* skull from top (top left), bottom (bottom left) and side (right). Tissue cuts are marked in blue and bone saw cuts are marked in red. **(C)** Experimental design of the tissue sectioning. Hemispheres were separated, the cerebellum removed, and the hemisphere placed with its medial side onto a cooled plate. The knife was moved along the bars (2 mm height), the rest of the hemisphere removed and placed onto the next plate. The plate was placed on dry ice until frozen and stored in a box at -80°C. **(D)** 15 mm lateral section depicting the extracted tissue blocks for single-cell sequencing and further treatment for smFISH. **(E)** 24 mm lateral section depicting the extracted tissue blocks for single cell sequencing and further treatment for smFISH.

Figure 2: Experimental procedure and snRNA-seq dataset

(A) Experimental design of the snRNA-seq measurement: tissue blocks from cortical areas V1 and V4 were dissected from sagittal slices of rhesus macaque brain, tissue was homogenized, nuclei purified using gradient centrifugation and neuronal nuclei were stained using NeuN with following FANS. Neuronal nuclei were sequenced using 10x Genomics assays. **(B)** Major neuronal families and their subtypes were detected using single nuclei RNA sequencing. UMAP representation of single nuclei transcriptomes is shown; nuclei are colored by their subtype. **(C)** UMAP representation of single nuclei, colored by cortical area V1 and V4. **(D)** Heat map depicting expression of markers for principal neuronal subtypes, log2 fold-change is plotted. **(E)** Heat map depicting expression of markers for inhibitory neuronal subtypes, log2 fold-change is plotted.

Figure 3: Compositional differences in cell types within visual areas

(A) Top plot: V1 layer 4 neuronal subtypes (in color) segregate from V4 subtypes (in grey) mostly by the presence of layer 4 V1-specific neuronal subtypes of L4_RORB family (L4_RORB_KCNH8_SEMA5A, L4_RORB_KCNH8_ARHGAP24, L4_RORB_KCNH8_KCNB2, L4_RORB_KCNH8_PARD3, L4_RORB_KCNH8_SPOCK3, L4_RORB_MET_CRISPLD1, L4_RORB_MET_KCNIP1); Bottom plot: Similarly, V4 layer 4 subtypes (in color) segregate from V1 layer 4 subtypes (in grey) mostly by the presence of V4-specific subtype L4_RORB_KCNH8_ABCA12. UMAP representation of nuclei transcriptomes is shown. **(B)** Expression of marker genes being selected for further smFISH analysis based on their expression

in cell clusters uniquely present in V1 layer 4. **(C)** V1 neuronal subtypes (orange) segregate from V4 subtypes (purple) in layer 4. **(D)** Relative number of principal neurons to GABAergic neurons (P:G ratio) in areas V1 and V4. Bar indicated the mean and 95% CI across samples. **(E)** Further change in neuronal composition between V1 and V4 evaluated by compositional data analysis. Cell types distinguishing composition of V1 and V4 samples and present in both regions are shown, region-specific subtypes mentioned above were omitted. The y-axis indicates the separating coefficient for each cell type, with values corresponding to neurons with increased abundance in V1 (top) and V4 (bottom). The boxplots and individual data points show uncertainty based on bootstrap resampling of samples and cells. Red line represents cut-off for significance of adjusted (by the Benjamini-Hochberg method) P values (significant cell types are above the line).

Figure 4: Enriched GO terms show similarities between unique V1 and V4 subtypes
(A) Heat map of the top three enriched GO terms for each annotated cell type, colored by $-\log_{10}$(adjusted p-value). GO term enrichment was calculated using a hypergeometric test and adjusted for multiple comparisons by the Benjamini–Hochberg procedure. Cell types unique to V1 are in green, unique to V4 in orange, and layer 4 types shared between V1 and V4 in purple. A red box was manually added to delineate a notable cluster encompassing all eight unique layer 4 neuronal subtypes, highlighting their shared enrichment in GO terms related to cell adhesion and neuron development (see main text for details). **(B)** Dot plot of genes annotated to the top three enriched GO terms for V1-unique (green) and V4-unique (orange) cell types, with dot size proportional to $-\log_{10}$(adjusted p-value) and color indicating average $\log_2$ fold-change.

Figure 5: Experimental design for quantitative smFISH
(A) Experimental design of the fluorescent in situ hybridization workflow. Tissue blocks were extracted from sagittal brain slices, sectioned into 10 µm sections, conducted to the RNAscope Multiplex Fluorescent V2 Assay, visualized utilizing a Leica SP8 confocal microscope and analyzed using the QuPath software. **(B)** Overview image showing an exemplary staining. Laminar patters for *CAMK2A*, *RORB*, the respective target and Nissl from the pia mater to the white matter. Fluorescent imaged from fourfold stain 10 µm thick section from V1. Scale bar: 200 µm. Brightfield image from 10 µm section from V1. Scale bar: 200 µm. **(C)** Exemplary single-color images from layer 4 in V1. DAPI nucleus staining: blue; *CAMK2A* hybridization: green; *RORB* hybridization: yellow and target hybridization: red. Segmentation: pink: negative; red: target +; blue: *CAMK2A* +; yellow: *RORB* +; dark green: *CAMK2A* + *RORB* +; orange: *RORB* + target+; purple: *CAMK2A* + target+; light green: *CAMK2A* + *RORB* + target+. Scale bar: 45 µm.

Figure 6: Gradient of unique subtypes of principal neurons along dorsal stream in visual cortex areas

771 **(A-D)** Percentage of *CAMK2A*+ *ROR*B+ target+ cells of *CAMK2A*+ *RORB*+ cells in layer 4 over
772 V1, V2, V4, MT, and TEO. Symbols represent data from 10 counting windows over n = 2 rhesus
773 macaques, circles represent monkey E and dots represent monkey S, bar represent means, error
774 bars represent 95% CIs. **(E)** Significance (single cells chi-square tested, Bonferroni corrected). **(F)**
775 Model showing the gradient development along the dorsal and ventral stream. Density of cell typed
776 decrease along the dorsal stream while along the ventral stream density of cell types decrease
777 until V4 but increase in TEO again.
778
779 **Figure 7: Enrichment of unique subtypes of principal neurons in layer 4**
780 **(A)** Overview image showing an exemplary staining. Laminar patters for DAPI, *RORB* and Nissl
781 from the pia mater to the white matter. Fluorescent images (DAPI and RORB) and brightfield image
782 (Nissl) from V1. Scale bar: 200 µm. **(B-E)** Percentage of *CAMK2A*+ *RORB*+ target+ cells of
783 *CAMK2A*+ *RORB*+ cells across layer 2/3, layer 4 and layer 5 for V1, V2, V4, MT and TEO. Symbols
784 represent data from 10 counting windows over n = 2 rhesus macaques, circles represent monkey
785 E and dots represent monkey S, bar represent means, error bars represent 95% CIs.

Figure 1

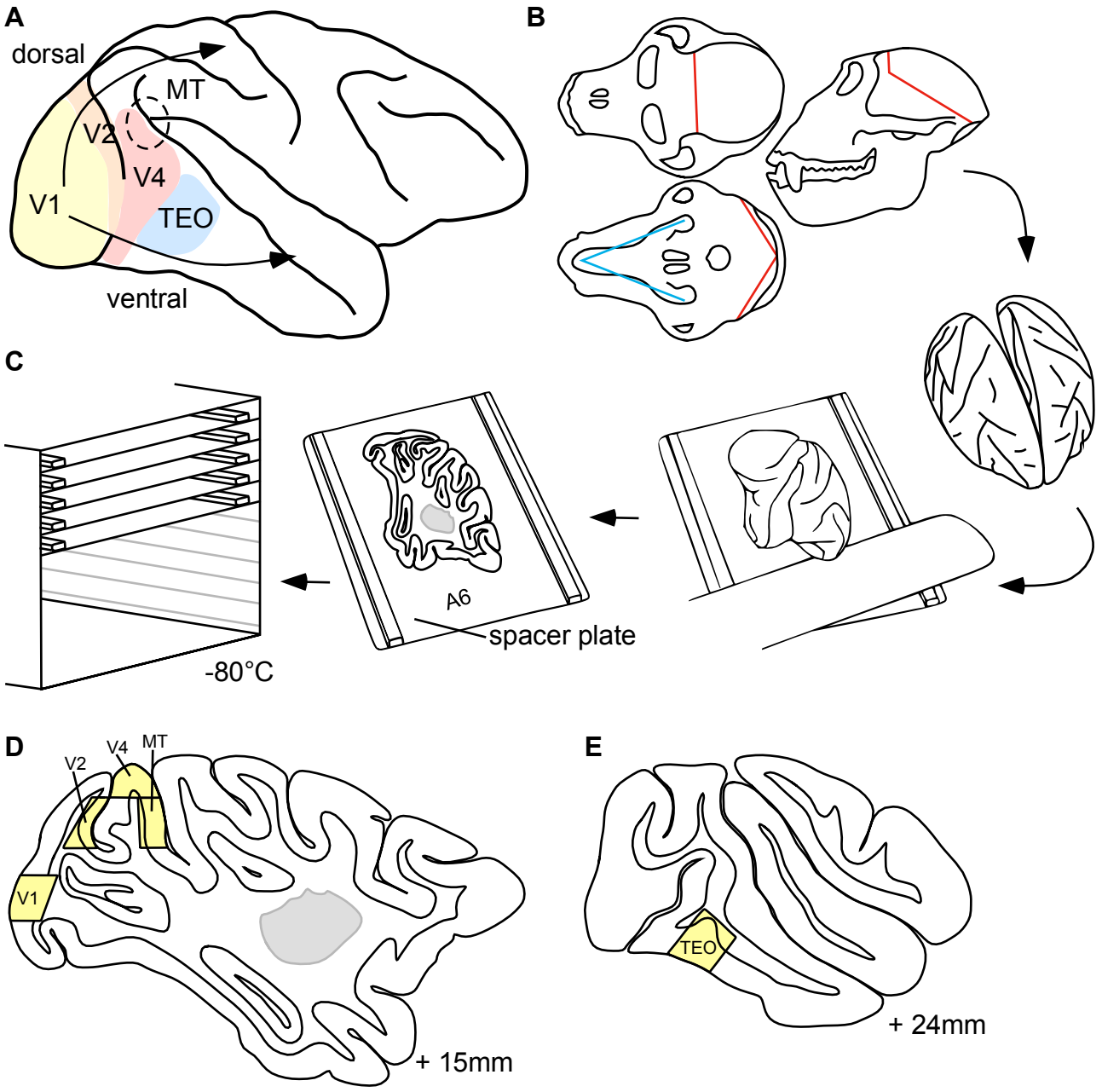
A
dorsal
MT
V2
V4
V1
TEO
ventral
B
C
A6
spacer plate
-80°C
D
V2
V4
MT
V1
+ 15mm
E
TEO
+ 24mm

Figure 2

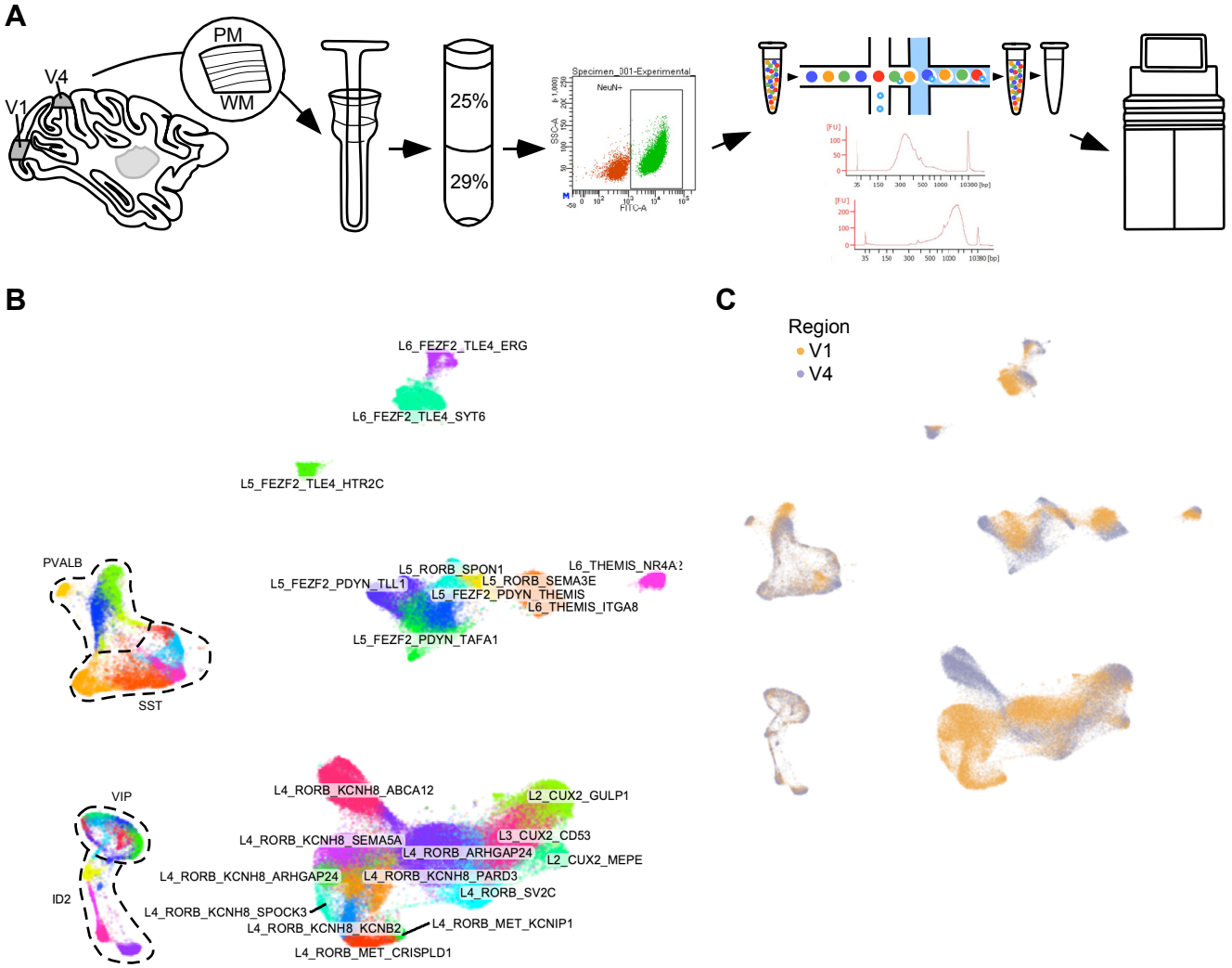
A
PM
WM
V4
V1
25%
29%
Specimen_001-Experimental
NeuN+
B
L6_FEZF2_TLE4_ERG
L6_FEZF2_TLE4_SYT6
L5_FEZF2_TLE4_HTR2C
PVALB
SST
L5_RORB_SPON1
L6_THEMIS_NR4A2
L5_FEZF2_PDYN_TLL1
L5_RORB_SEMA3E
L5_FEZF2_PDYN_THEMIS
L6_THEMIS_ITGA8
L5_FEZF2_PDYN_TAFA1
VIP
ID2
L4_RORB_KCNH8_ABCA12
L2_CUX2_GULP1
L4_RORB_KCNH8_SEMA5A
L3_CUX2_CD53
L4_RORB_ARHGAP24
L2_CUX2_MEPE
L4_RORB_KCNH8_ARHGAP24
L4_RORB_KCNH8_PARD3
L4_RORB_SV2C
L4_RORB_KCNH8_SPOCK3
L4_RORB_KCNH8_KCNB2
L4_RORB_MET_KCNIP1
L4_RORB_MET_CRISPLD1
C
Region
V1
V4

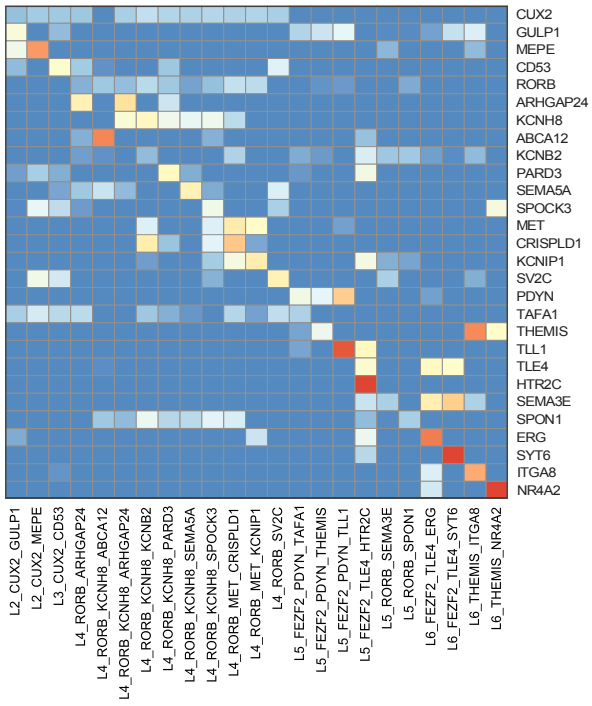
D
CUX2
GULP1
MEPE
CD53
RORB
ARHGAP24
KCNH8
ABCA12
KCNB2
PARD3
SEMA5A
SPOCK3
MET
CRISPLD1
KCNIP1
SV2C
PDYN
TAFA1
THEMIS
TLL1
TLE4
HTR2C
SEMA3E
SPON1
ERG
SYT6
ITGA8
NR4A2
L2_CUX2_GULP1
L2_CUX2_MEPE
L3_CUX2_CD53
L4_RORB_ARHGAP24
L4_RORB_KCNH8_ABCA12
L4_RORB_KCNH8_ARHGAP24
L4_RORB_KCNH8_KCNB2
L4_RORB_KCNH8_PARD3
L4_RORB_KCNH8_SEMA5A
L4_RORB_KCNH8_SPOCK3
L4_RORB_MET_CRISPLD1
L4_RORB_MET_KCNIP1
L4_RORB_SV2C
L5_FEZF2_PDYN_TAFA1
L5_FEZF2_PDYN_THEMIS
L5_FEZF2_PDYN_TLL1
L5_FEZF2_TLE4_HTR2C
L5_RORB_SEMA3E
L5_RORB_SPON1
L6_FEZF2_TLE4_ERG
L6_FEZF2_TLE4_SYT6
L6_THEMIS_ITGA8
L6_THEMIS_NR4A2

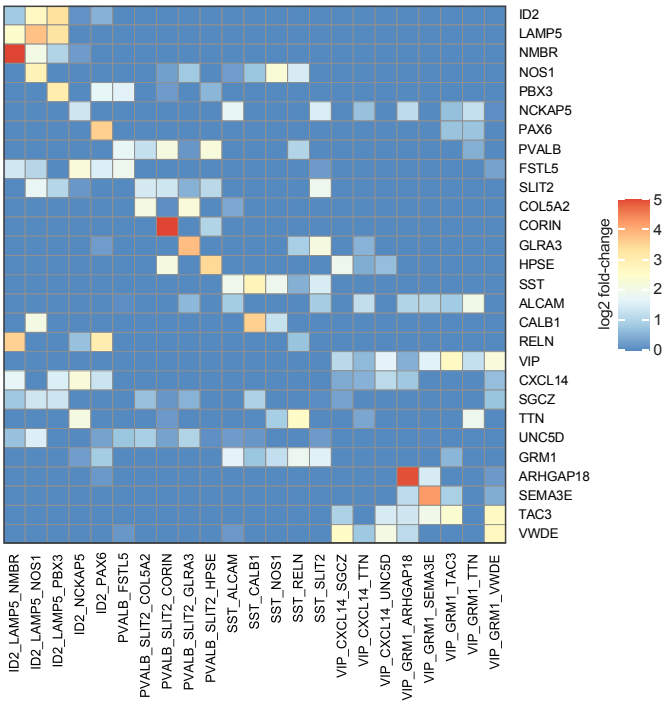
E
ID2
LAMP5
NMBR
NOS1
PBX3
NCKAP5
PAX6
PVALB
FSTL5
SLIT2
COL5A2
CORIN
GLRA3
HPSE
SST
ALCAM
CALB1
RELN
VIP
CXCL14
SGCZ
TTN
UNC5D
GRM1
ARHGAP18
SEMA3E
TAC3
VWDE
log2 fold-change
5
4
3
2
1
0
ID2_LAMP5_NMBR
ID2_LAMP5_NOS1
ID2_LAMP5_PBX3
ID2_NCKAP5
ID2_PAX6
PVALB_FSTL5
PVALB_SLIT2_COL5A2
PVALB_SLIT2_CORIN
PVALB_SLIT2_GLRA3
PVALB_SLIT2_HPSE
SST_ALCAM
SST_CALB1
SST_NOS1
SST_RELN
SST_SLIT2
VIP_CXCL14_SGCZ
VIP_CXCL14_TTN
VIP_CXCL14_UNC5D
VIP_GRM1_ARHGAP18
VIP_GRM1_SEMA3E
VIP_GRM1_TAC3
VIP_GRM1_TTN
VIP_GRM1_VWDE

Figure 3

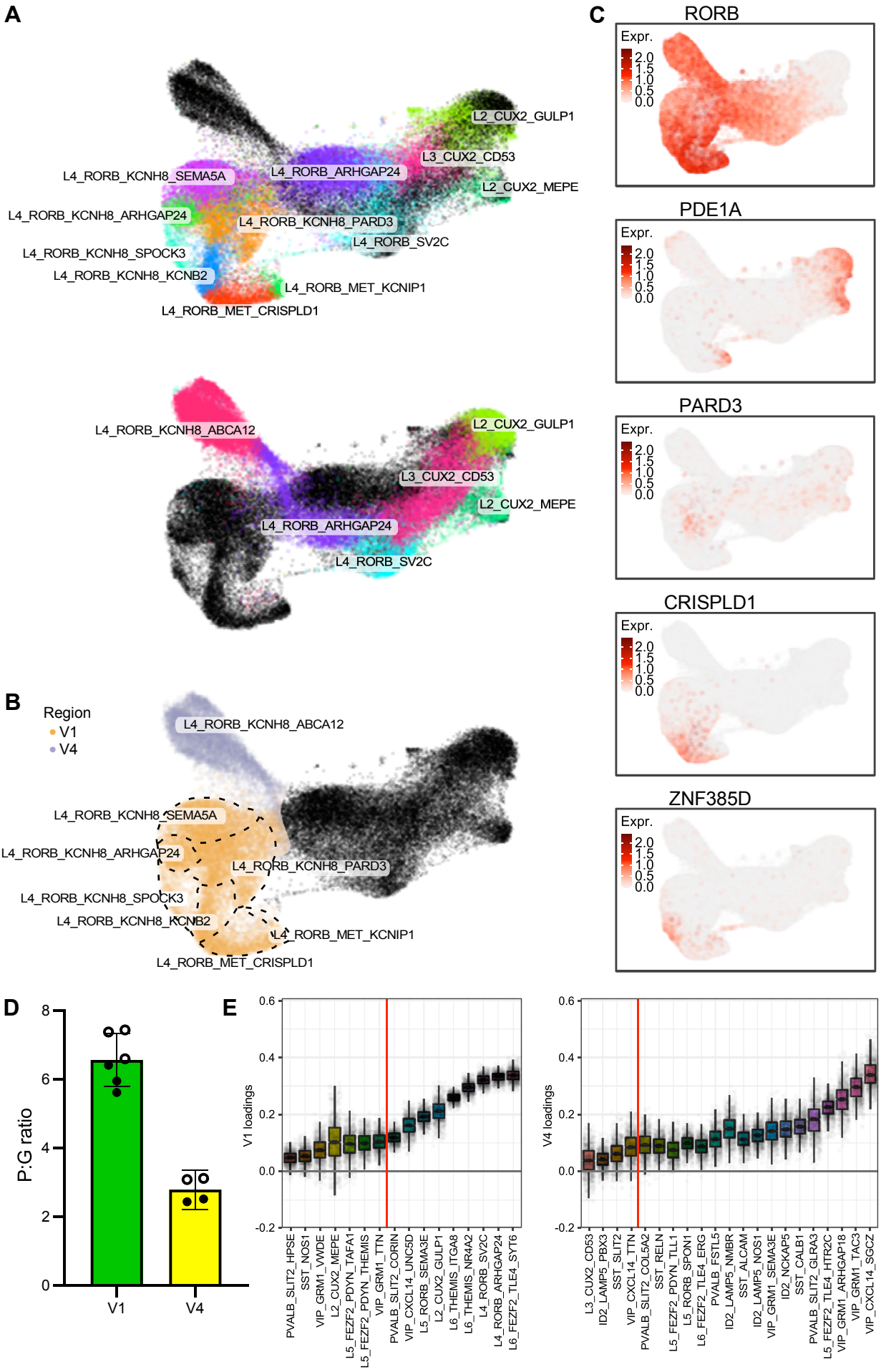
A
L2_CUX2_GULP1
L3_CUX2_CD53
L4_RORB_KCNH8_SEMA5A
L4_RORB_ARHGAP24
L2_CUX2_MEPE
L4_RORB_KCNH8_ARHGAP24
L4_RORB_KCNH8_PARD3
L4_RORB_SV2C
L4_RORB_KCNH8_SPOCK3
L4_RORB_KCNH8_KCNB2
L4_RORB_MET_KCNIP1
L4_RORB_MET_CRISPLD1
L4_RORB_KCNH8_ABCA12
L2_CUX2_GULP1
L3_CUX2_CD53
L2_CUX2_MEPE
L4_RORB_ARHGAP24
L4_RORB_SV2C
B
Region
V1
V4
L4_RORB_KCNH8_ABCA12
L4_RORB_KCNH8_SEMA5A
L4_RORB_KCNH8_ARHGAP24
L4_RORB_KCNH8_PARD3
L4_RORB_KCNH8_SPOCK3
L4_RORB_KCNH8_KCNB2
L4_RORB_MET_KCNIP1
L4_RORB_MET_CRISPLD1
C
RORB
PDE1A
PARD3
CRISPLD1
ZNF385D
Expr.
2.0
1.5
1.0
0.5
0.0
D
P:G ratio
8
6
4
2
0
V1
V4
E
V1 loadings
0.6
0.4
0.2
0.0
-0.2
PVALB_SLIT2_HPSE
SST_NOS1
VIP_GRM1_VWDE
L2_CUX2_MEPE
L5_FEZF2_PDYN_TAFA1
L5_FEZF2_PDYN_THEMIS
VIP_GRM1_TTN
PVALB_SLIT2_CORIN
VIP_CXCL14_UNC5D
L5_RORB_SEMA3E
L2_CUX2_GULP1
L6_THEMIS_ITGA8
L6_THEMIS_NR4A2
L4_RORB_SV2C
L4_RORB_ARHGAP24
L6_FEZF2_TLE4_SYT6
V4 loadings
L3_CUX2_CD53
ID2_LAMP5_PBX3
SST_SLIT2
VIP_CXCL14_TTN
PVALB_SLIT2_COL5A2
SST_RELN
L5_FEZF2_PDYN_TLL1
L5_RORB_SPON1
L6_FEZF2_TLE4_ERG
PVALB_FSTL5
ID2_LAMP5_NMBR
SST_ALCAM
ID2_LAMP5_NOS1
VIP_GRM1_SEMA3E
ID2_NCKAP5
SST_CALB1
PVALB_SLIT2_GLRA3
L5_FEZF2_TLE4_HTR2C
VIP_GRM1_ARHGAP18
VIP_GRM1_TAC3
VIP_CXCL14_SGCZ

Figure 4

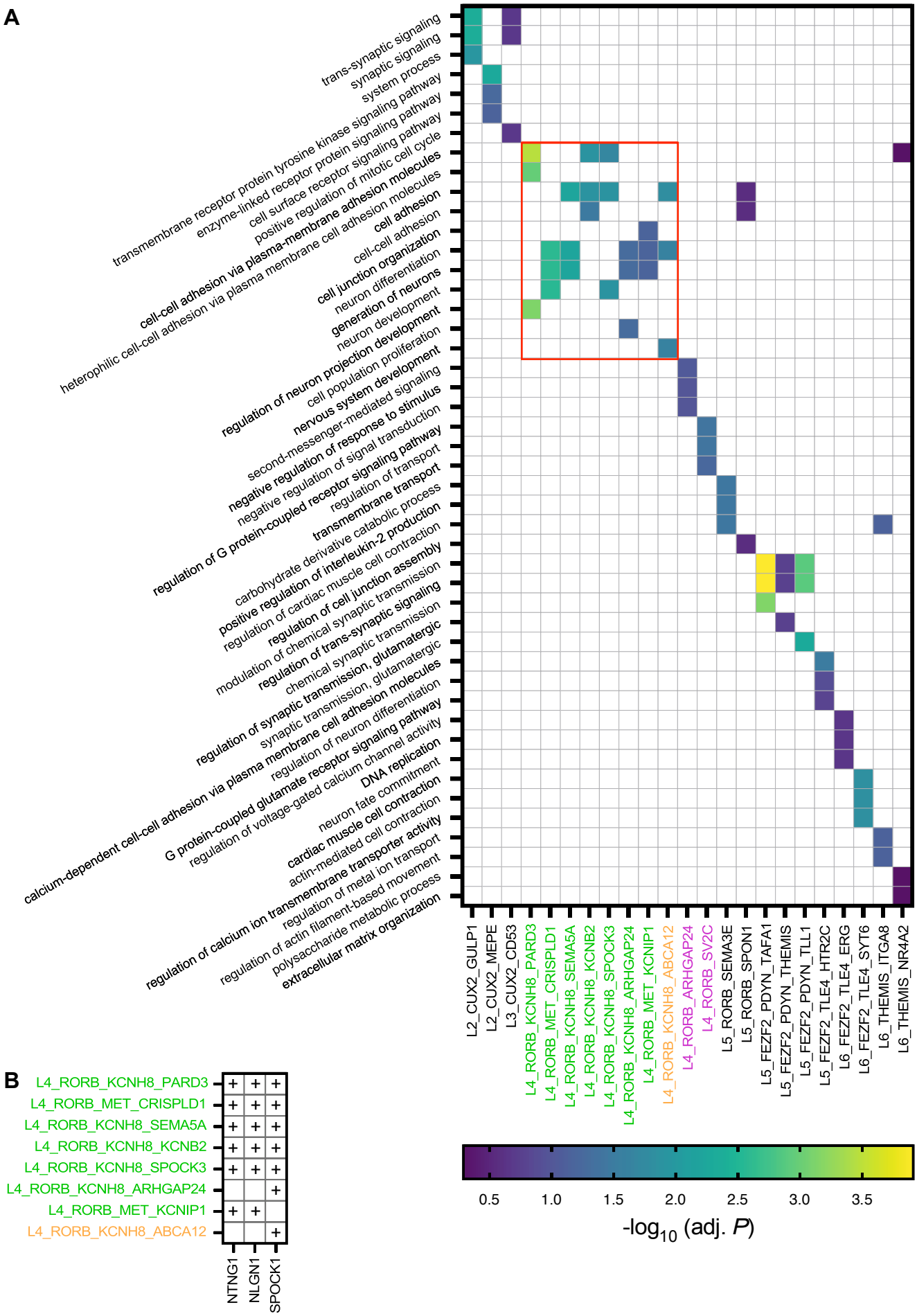
A
trans-synaptic signaling
synaptic signaling
system process
transmembrane receptor protein tyrosine kinase signaling pathway
enzyme-linked receptor protein signaling pathway
cell surface receptor signaling pathway
positive regulation of mitotic cell cycle
cell-cell adhesion via plasma-membrane adhesion molecules
heterophilic cell-cell adhesion via plasma membrane cell adhesion molecules
cell adhesion
cell-cell adhesion
cell junction organization
neuron differentiation
generation of neurons
neuron development
regulation of neuron projection development
cell population proliferation
nervous system development
second-messenger-mediated signaling
negative regulation of response to stimulus
negative regulation of signal transduction
regulation of G protein-coupled receptor signaling pathway
regulation of transport
transmembrane transport
carbohydrate derivative catabolic process
positive regulation of interleukin-2 production
regulation of cardiac muscle cell contraction
regulation of cell junction assembly
modulation of chemical synaptic transmission
regulation of trans-synaptic signaling
chemical synaptic transmission
regulation of synaptic transmission, glutamatergic
synaptic transmission, glutamatergic
calcium-dependent cell-cell adhesion via plasma membrane cell adhesion molecules
regulation of neuron differentiation
G protein-coupled glutamate receptor signaling pathway
regulation of voltage-gated calcium channel activity
DNA replication
neuron fate commitment
cardiac muscle cell contraction
actin-mediated cell contraction
regulation of calcium ion transmembrane transporter activity
regulation of metal ion transport
regulation of actin filament-based movement
polysaccharide metabolic process
extracellular matrix organization
L2_CUX2_GULP1
L2_CUX2_MEPE
L3_CUX2_CD53
L4_RORB_KCNH8_PARD3
L4_RORB_MET_CRISPLD1
L4_RORB_KCNH8_SEMA5A
L4_RORB_KCNH8_KCNB2
L4_RORB_KCNH8_SPOCK3
L4_RORB_KCNH8_ARHGAP24
L4_RORB_MET_KCNIP1
L4_RORB_KCNH8_ABCA12
L4_RORB_ARHGAP24
L4_RORB_SV2C
L5_RORB_SEMA3E
L5_RORB_SPON1
L5_FEZF2_PDYN_TAFA1
L5_FEZF2_PDYN_THEMIS
L5_FEZF2_PDYN_TLL1
L5_FEZF2_TLE4_HTR2C
L6_FEZF2_TLE4_ERG
L6_FEZF2_TLE4_SYT6
L6_THEMIS_ITGA8
L6_THEMIS_NR4A2
0.5
1.0
1.5
2.0
2.5
3.0
3.5
-log10 (adj. P)
B
L4_RORB_KCNH8_PARD3 + + +
L4_RORB_MET_CRISPLD1 + + +
L4_RORB_KCNH8_SEMA5A + + +
L4_RORB_KCNH8_KCNB2 + + +
L4_RORB_KCNH8_SPOCK3 + + +
L4_RORB_KCNH8_ARHGAP24 +
L4_RORB_MET_KCNIP1 + +
L4_RORB_KCNH8_ABCA12 +
NTNG1
NLGN1
SPOCK1

Figure 5

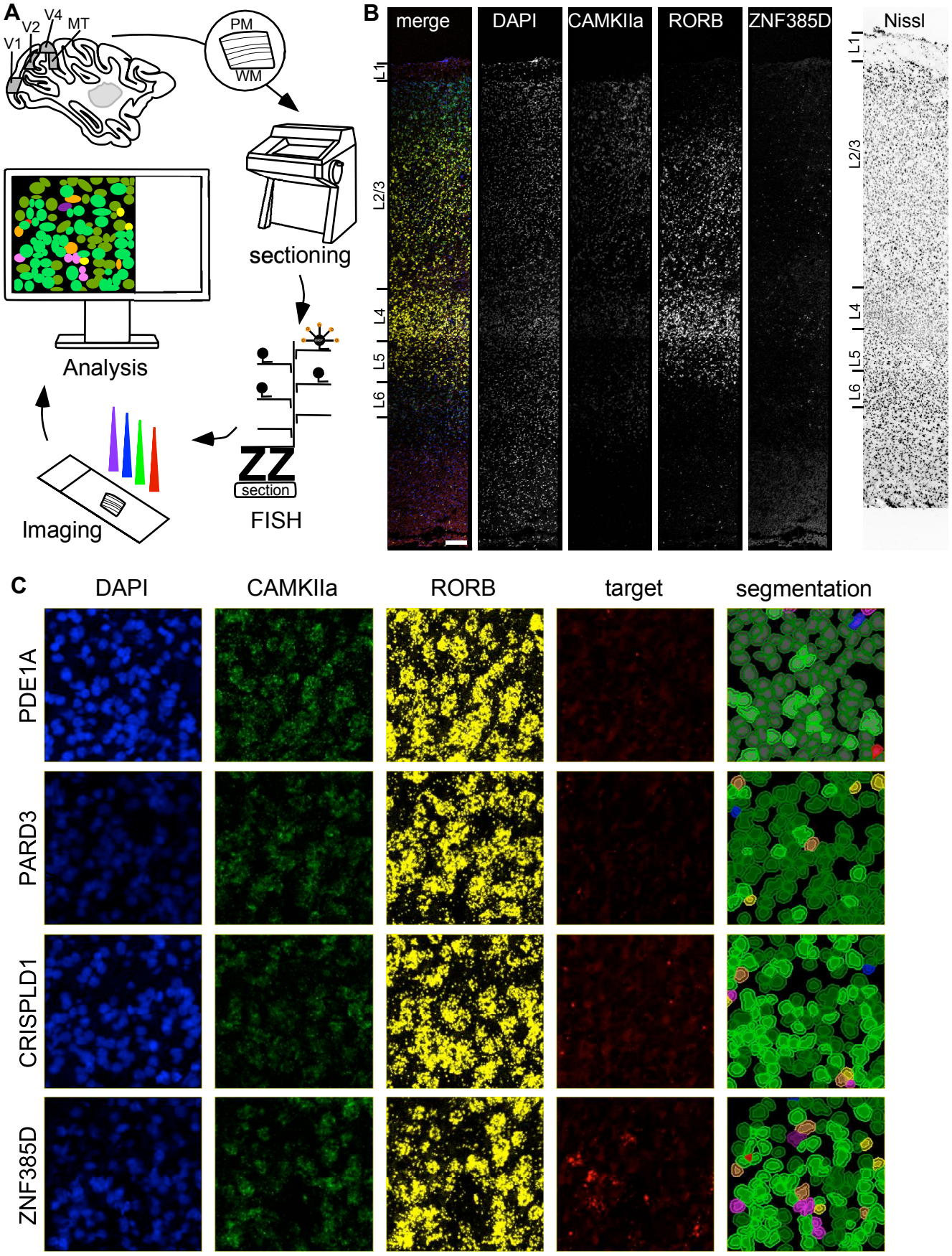
A
V1
V2
V4
MT
PM
WM
sectioning
Analysis
section
FISH
Imaging
B
merge
DAPI
CAMKIIa
RORB
ZNF385D
Nissl
L1
L2/3
L4
L5
L6
C
DAPI
CAMKIIa
RORB
target
segmentation
PDE1A
PARD3
CRISPLD1
ZNF385D

Figure 6

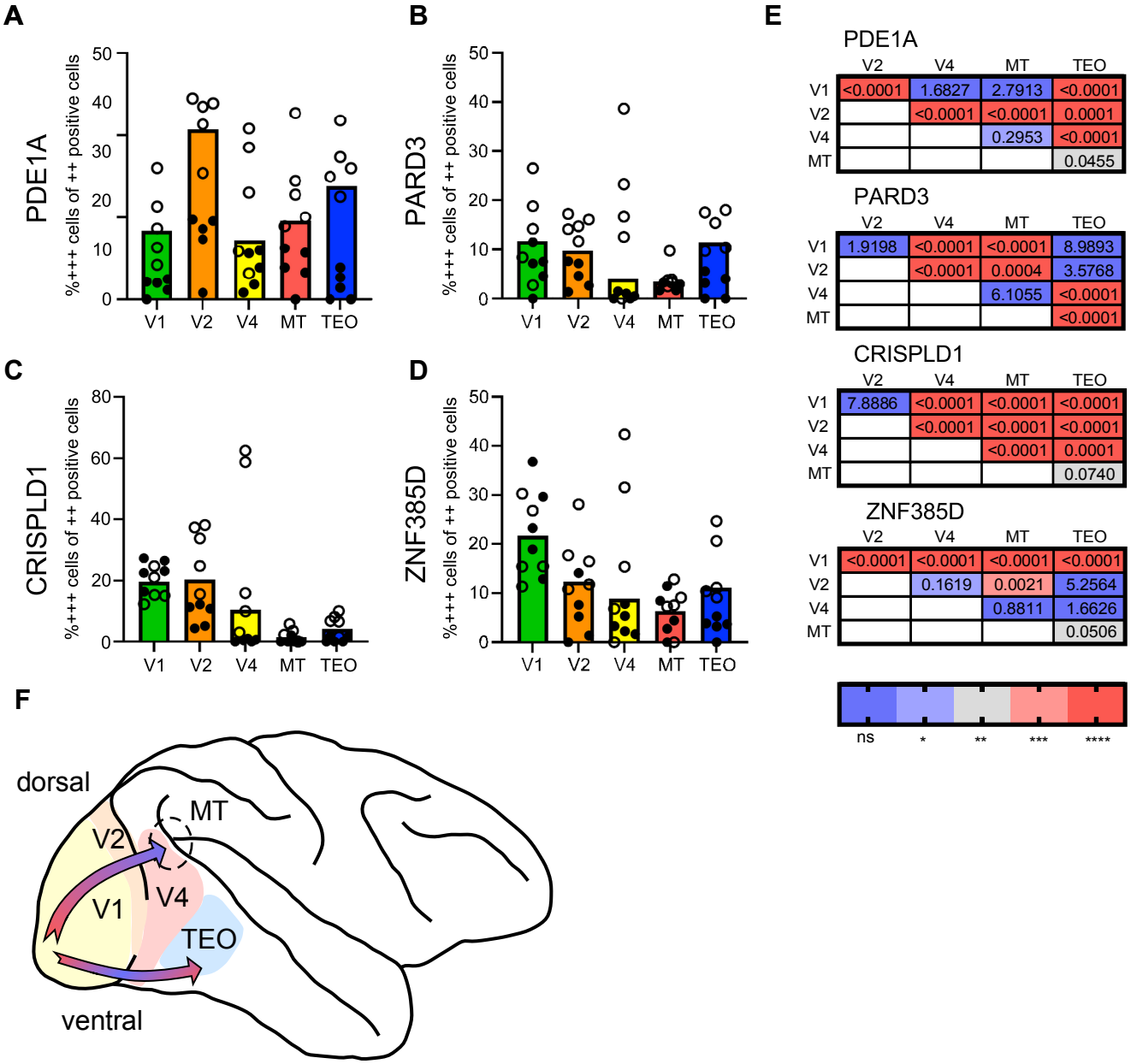
A
PDE1A
%+++ cells of ++ positive cells
0
10
20
30
40
50
V1
V2
V4
MT
TEO
B
PARD3
%+++ cells of ++ positive cells
0
10
20
30
40
50
V1
V2
V4
MT
TEO
C
CRISPLD1
%+++ cells of ++ positive cells
0
20
40
60
80
V1
V2
V4
MT
TEO
D
ZNF385D
%+++ cells of ++ positive cells
0
10
20
30
40
50
V1
V2
V4
MT
TEO
E
PDE1A
V2 V4 MT TEO
V1 <0.0001 1.6827 2.7913 <0.0001
V2 <0.0001 <0.0001 0.0001
V4 0.2953 <0.0001
MT 0.0455
PARD3
V2 V4 MT TEO
V1 1.9198 <0.0001 <0.0001 8.9893
V2 <0.0001 0.0004 3.5768
V4 6.1055 <0.0001
MT <0.0001
CRISPLD1
V2 V4 MT TEO
V1 7.8886 <0.0001 <0.0001 <0.0001
V2 <0.0001 <0.0001 <0.0001
V4 <0.0001 0.0001
MT 0.0740
ZNF385D
V2 V4 MT TEO
V1 <0.0001 <0.0001 <0.0001 <0.0001
V2 0.1619 0.0021 5.2564
V4 0.8811 1.6626
MT 0.0506
ns
*
**
***
****
F
dorsal
MT
V2
V1
V4
TEO
ventral

Figure 7

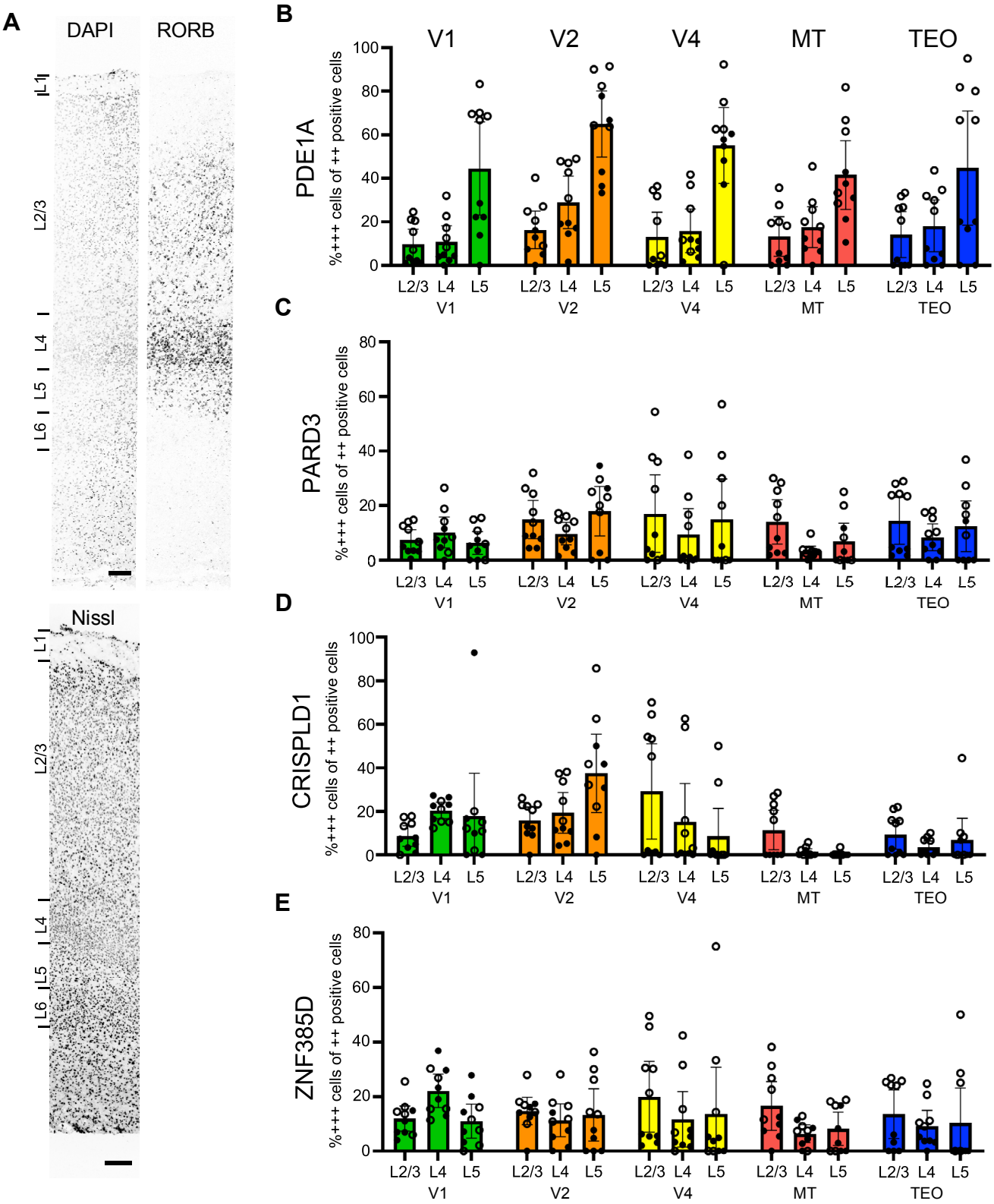
A
DAPI
RORB
Nissl
L1
L2/3
L4
L5
L6
B
PDE1A
C
PARD3
D
CRISPLD1
E
ZNF385D
V1
V2
V4
MT
TEO
%+++ cells of ++ positive cells
L2/3
L4
L5